J|A|C|S ARTICLES

Published on Web 02/05/2010

A Series of Peroxomanganese(III) Complexes Supported by Tetradentate Aminopyridyl Ligands: Detailed Spectroscopic and Computational Studies

Robert A. Geiger, Swarup Chattopadhyay, Victor W. Day, and Timothy A. Jackson*

Department of Chemistry and Center for Environmentally Beneficial Catalysis, University of Kansas, Lawrence, Kansas 66045

Received December 3, 2009; E-mail: taj@ku.edu

Abstract: A set of four $[Mn^{II}(L^7py_2^R)]^{2+}$ complexes, supported by the tetradentate 1,4-bis(2-pyridylmethyl)-1,4-diazepane ligand and derivatives with pyridine substituents in the 5 (R = Br) and 6 positions (R = Me and MeO), are reported. X-ray crystal structures of these complexes all show the $L^7py_2^R$ ligands bound to give a *trans* complex. Treatment of these Mn^{II} precursors with either H_2O_2/Et_3N or KO_2 in MeCN at −40 °C results in the formation of peroxomanganese complexes $[Mn^{III}(O_2)(L^7py_2^R)]^+$ differing only in the identity of the pyridine ring substituent. The electronic structures of two of these complexes, $[Mn^{III}(O_2)(L^7py_2^H)]^+$ and $[Mn^{III}(O_2)(L^7py_2^{Me})]^+$, were examined in detail using electronic absorption, low-temperature magnetic circular dichroism (MCD) and variable-temperature variable-field (VTVH) MCD spectroscopies to determine ground-state zero-field splitting (ZFS) parameters and electronic transition energies, intensities, and polarizations. DFT and TD-DFT computations were used to validate the structures of $[Mn^{III}(O_2)(L^7py_2^H)]^+$ and $[Mn^{III}(O_2)(L^7py_2^{Me})]^+$, further corroborating their assignment as peroxomanganese(III) species. While these complexes exhibit similar ZFS parameters, their low-temperature MCD spectra reveal significant shifts in electronic transition energies that are correlated to differences in $Mn-O_2$ interactions among these complexes. Taken together, these results indicate that, while the $[Mn^{III}(O_2)(L^7py_2^H)]^+$ complex exhibits symmetric $Mn-O_{peroxo}$ bond lengths, consistent with a side-on bound peroxo ligand, the peroxo ligand of the $[Mn^{III}(O_2)(L^7py_2^{Me})]^+$ complex is bound in a more end-on fashion, with asymmetric $Mn-O_{peroxo}$ distances. This difference in binding mode is rationalized in terms of the greater electron-donating abilities of the methyl-appended pyridines and suggests a simple way to modulate $Mn^{III}-O_2$ bonding through ligand perturbations.

Introduction

Manganese centers that react with oxygen and its reduced derivatives play important roles in biological systems, including the detoxification of superoxide and hydrogen peroxide and the bioremediation of aromatics.[1−5] Such manganese centers are also of interest for synthetic applications, as they have been shown to mediate useful oxygenation reactions, including olefin epoxidation, C−H bond hydroxylation, and alcohol oxidation.[6−12] While the elucidation of the mechanisms of these systems remains the subject of much current work, the importance of peroxo-level intermediates has been underscored by several reports. For example, the enzyme manganese superoxide dismutase (MnSOD), which functions to disproportionate superoxide to dioxygen and water, forms a product-inhibited complex under high superoxide concentrations that has been proposed as a peroxomanganese(III) adduct.[13,14] With respect to synthetic manganese catalysts that activate hydrogen peroxide, (hydro)-peroxomanganese intermediates are often proposed to precede high-valent oxomanganese adducts invoked as active oxidants.[6,9] Alternatively, in some cases, peroxomanganese intermediates have been proposed as the active species for substrate oxidation.[15] Thus, fundamental studies of peroxomanganese(III) intermediates should advance the current level of understanding of manganese centers important in biological and synthetic systems.

(1) Emerson, J. P.; Kovaleva, E. G.; Farquhar, E. R.; Lipscomb, J. D.; Que, L. Jr. *Proc. Natl. Acad. Sci. U.S.A.* **2008**, *105*, 7347–7352.
(2) Grove, L. E.; Brunold, T. C. *Comments Inorg. Chem.* **2008**, *29*, 134–168.
(3) Gunderson, W. A.; Zatsman, A. I.; Emerson, J. P.; Farquhar, E. R.; Que, L. Jr.; Lipscomb, J. D.; Hendrich, M. P. *J. Am. Chem. Soc.* **2008**, *130*, 14465–14467.
(4) Miller, A.-F. *Curr. Opin. Chem. Biol.* **2004**, *8*, 162–168.
(5) Wu, A. J.; Penner-Hahn, J. E.; Pecoraro, V. L. *Chem. Rev.* **2004**, *104*, 903–938.
(6) Hage, R.; Lienke, A. *Angew. Chem., Int. Ed.* **2006**, *45*, 206–222.
(7) Hage, R.; Lienke, A. *J. Mol. Catal. A: Chem.* **2006**, *251*, 150–158.
(8) Lane, B. S.; Burgess, K. *Chem. Rev.* **2003**, *103*, 2457–2473.
(9) Sibbons, K.; Shastri, K.; Watkinson, M. *Dalton Trans.* **2006**, 645–661.
(10) Wang, S. H.; Mandimutsira, B. S.; Todd, R.; Ramdhanie, B.; Fox, J. P.; Goldberg, D. P. *J. Am. Chem. Soc.* **2003**, *126*, 18–19.
(11) Lansky, D. E.; Goldberg, D. P. *Inorg. Chem.* **2006**, *45*, 5119–5125.
(12) Parsell, T. H.; Yang, M.-Y.; Borovik, A. S. *J. Am. Chem. Soc.* **2009**, *131*, 2762–2763.
(13) Bull, C.; Niederhoffer, E. C.; Yoshida, T.; Fee, J. A. *J. Am. Chem. Soc.* **1991**, *113*, 4069–4076.
(14) Hearn, A. S.; Tu, C. K.; Nick, H. S.; Silverman, D. N. *J. Biol. Chem.* **1999**, *274*, 24457–24460.
(15) Yin, G.; Buchalova, M.; Danby, A. M.; Perkins, C. M.; Kitko, D.; Carter, J. D.; Scheper, W. M.; Busch, D. H. *Inorg. Chem.* **2006**, *45*, 3467–3474.

 © 2010 American Chemical Society

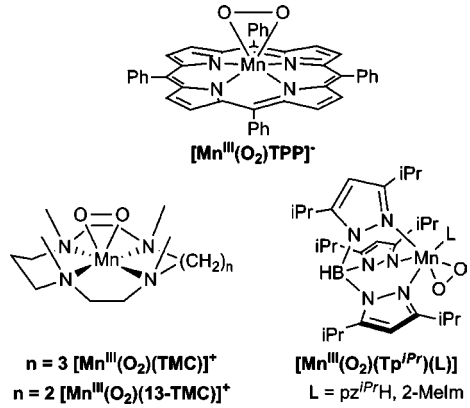

Figure 1. Representations of the molecular structures of peroxomanganese(III) adducts characterized by X-ray crystallography.[19−22,24]

To date, a handful of peroxomanganese(III) species have been reported,[16−22] and these have typically been generated by treating Mn^{II} precursors with H_2O_2 or KO_2. In only one case has O_2 been used as the oxidant.[18] Because of their limited thermal stabilities, low temperatures (<0 °C) are often required to stabilize these intermediates. X-ray diffraction (XRD) structures for the more stable complexes have revealed O−O bond lengths ranging from 1.40 to 1.43 Å,[19−22] firmly establishing the peroxo assignment. The Mn−O bond lengths vary from 1.841 to 1.901 Å, similar to Mn^{III}−OH distances found in synthetic complexes and Mn enzymes.[23] The longer Mn−O bond lengths (∼1.89 Å) were observed for adducts reported by the groups of Valentine and Nam, who respectively used the dianionic TPP (TPP = tetraphenylporphyrin) and neutral TMC (TMC = tetramethylcyclam) ligands that both provide four coplanar N donors (Figure 1).[20,22] Mn^{III}−O_2 species supported by the facially coordinating, monoanionic Tp^{iPr} (Tp^{iPr} = tris(3,5-diisopropylpyrazolyl)borate) ligand show a degree of variation in Mn−O bond lengths (1.84−1.88 Å), with the longer distances attributed to H-bonding interactions proposed to have a stabilizing effect on the Mn^{III}−O_2 unit.[19,21] The thermal stabilities of these complexes vary remarkably, with the Mn^{III}−O_2 adducts of TMC and Me-TPEN (Me-TPEN = *N*-methyl-*N*,*N*′,*N*′-tris(2-pyridylmethyl)ethane-1,2-diamine) providing the extremes with room temperature half-lives of ∼5 h and ∼30 min, respectively. The unusual stability of the TMC complex was attributed to steric crowding around the peroxo group from the *N*-methyl substituents of the TMC macrocycle.

Characteristic spectroscopic features of Mn^{III}−O_2 complexes include weak absorption bands in the visible region, the energies and intensities of which are dependent on the supporting ligand. For example, Mn^{III}−O_2 adducts of the Tp^{iPr} and Me-TPEN ligands show one prominent band centered at ∼560 − 590 nm with more intense features at <400 nm. The corresponding TMC complex displays two bands of differing intensities at ∼630 and 453 nm. Given their low intensities, these bands likely arise from Mn^{III} *d*−*d* transitions, though it should be noted that weak charge-transfer (CT) bands are observed for Fe^{III}−O_2 adducts at ∼700 nm ($\epsilon \approx 500\ M^{-1}\ cm^{-1}$).[25] Resonance Raman experiments exciting into the visible bands of Mn^{III}−O_2 adducts have not yet permitted observation of the O−O or Mn−O stretching modes,[16,20] consistent with the assignment of these bands as *d*−*d* transitions. This is in contrast to peroxoiron(III) complexes that are quite amenable to interrogation using resonance Raman spectroscopy. IR spectroscopy was used to obtain ν_{OO} frequencies for four Mn^{III}−O_2 adducts, which fall within the narrow range of ∼885−896 cm^{-1}. These frequencies are blue-shifted by ∼70 cm^{-1} compared to those of high-spin Fe^{III}−O_2 adducts,[25] suggesting a stronger O−O bond in the Mn^{III}−O_2 adducts. Lack of corresponding information regarding the Mn−O_{peroxo} bond strength represents a crucial gap in knowledge, as a comparison of the relative Mn−O and O−O bond strengths is expected to be of key importance in understanding the reactivities of these complexes.

Scheme 1

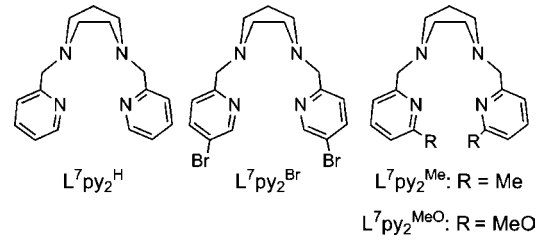

Reactivity studies of Mn^{III}−O_2 adducts have shown that the peroxo ligand is nucleophilic, though not as much so as in corresponding peroxoiron(III) adducts.[26] A characteristic reaction is the deformylation of aldehydes, as demonstrated for the $[Mn^{III}(O_2)(TMC)]^+$ and $[Mn^{III}(O_2)(H_3bupa)]^-$ complexes.[18,20] Studies of a series of $[Mn^{III}(O_2)(13\text{-}TMC)(X)]^+$ complexes, where the axial ligand X = CN^-, NCS^-, $CF_3CO_2^-$, and N_3^-, or was absent, revealed that the identity of the axial ligand can affect the rate of aldehyde deformylation by nearly 3 orders of magnitude.[24] It was proposed that strongly electron-donating *trans* ligands convert the side-on peroxo ligand to a more end-on geometry, with nonequivalent Mn−O bond lengths. While the reactivities of peroxomanganese(III) complexes have been the subject of several in-depth studies, the electronic structure of these complexes has remained comparatively unexplored.

In this paper we report the generation and characterization of four peroxomanganese(III) adducts supported by derivatives of the linear tetradentate $L^7py_2^R$ (L^7py_2 = 1,4-bis(2-pyridylmethyl)-1,4-diazepane) ligands (Scheme 1) that differ only with respect to the identity of pyridine ring substituents (R = H, Br, Me, and MeO). X-ray diffraction (XRD), ESI-MS, and ^1H NMR experiments have been used to characterize the solid-state and solution properties of the corresponding manganese(II) precursors. For all complexes, the XRD structures show the $L^7py_2^R$ ligand bound in a *trans* conformation, which we propose plays an important role in governing the reactivity of these complexes

(16) Groni, S.; Blain, G.; Guillot, R.; Policar, C.; Anxolabéhère-Mallart, E. *Inorg. Chem.* **2007**, *46*, 1951–1953.
(17) Groni, S.; Dorlet, P.; Blain, G.; Bourcier, S.; Guillot, R.; Anxolabéhère-Mallart, E. *Inorg. Chem.* **2008**, *47*, 3166–3172.
(18) Shook, R. L.; Gunderson, W. A.; Greaves, J.; Ziller, J. W.; Hendrich, M. P.; Borovik, A. S. *J. Am. Chem. Soc.* **2008**, *130*, 8888–8889.
(19) Kitajima, N.; Komatsuzaki, H.; Hikichi, S.; Osawa, M.; Moro-oka, Y. *J. Am. Chem. Soc.* **1994**, *116*, 11596–11597.
(20) Seo, M. S.; Kim, J. Y.; Annaraj, J.; Kim, Y.; Lee, Y.-M.; Kim, S.-J.; Kim, J.; Nam, W. *Angew. Chem., Int. Ed.* **2007**, *46*, 377–380.
(21) Singh, U. P.; Sharma, A. K.; Hikichi, S.; Komatsuzaki, H.; Moro-oka, Y.; Akita, M. *Inorg. Chim. Acta* **2006**, *359*, 4407–4411.
(22) VanAtta, R. B.; Strouse, C. E.; Hanson, L. K.; Valentine, J. S. *J. Am. Chem. Soc.* **1987**, *109*, 1425–1434.
(23) Jackson, T. A.; Brunold, T. C. *Acc. Chem. Res.* **2004**, *37*, 461–470.
(24) Annaraj, J.; Cho, J.; Lee, Y.-M.; Kim, S. Y.; Latifi, R.; de Visser, S. P.; Nam, W. *Angew. Chem., Int. Ed.* **2009**, *48*, 4150–4153.
(25) Costas, M.; Mehn, M. P.; Jensen, M. P.; Que, L. Jr. *Chem. Rev.* **2004**, *104*, 939–986.
(26) Sisemore, M. F.; Selke, M.; Burstyn, J. N.; Valentine, J. S. *Inorg. Chem.* **1997**, *36*, 979–984.

with hydrogen peroxide. The four peroxomanganese(III) complexes $[Mn^{III}(O_2)(L^7py_2^H)]^+$, $[Mn^{III}(O_2)(L^7py_2^{Br})]^+$, $[Mn^{III}(O_2)(L^7py_2^{Me})]^+$, $[Mn^{III}(O_2)(L^7py_2^{MeO})]^+$ were generated using cryogenic techniques and characterized by ESI-MS and electronic absorption spectroscopy. The electronic structures of the $[Mn^{III}(O_2)(L^7py_2^H)]^+$ and $[Mn^{III}(O_2)(L^7py_2^{Me})]^+$ complexes were investigated in more detail using low-temperature magnetic circular dichroism (MCD) and variable-temperature, variable-field (VTVH) MCD spectroscopies. Whereas fits of VTVH MCD data collected for these samples revealed similar ground-state zero-field splitting parameters, the electronic absorption and MCD spectra display key differences in $d-d$ and charge-transfer transition energies, indicating structural and/or electronic perturbations among these complexes. Using a framework provided by density functional theory (DFT) computations, these spectroscopic perturbations were related to differences in $Mn^{III}-O_2$ bonding among these complexes. Specifically, these data suggest that the presence of electron-rich substituents supports more asymmetric (i.e., more end-on) peroxo ligands. Together, these combined experimental and theoretical studies provide the first detailed investigation of the electronic structures of peroxomanganese(III) adducts and offer a basis for correlating spectroscopic features with $Mn^{III}-O_2$ bonding.

Materials and Methods

Materials. All chemicals obtained from commercial vendors were ACS reagent-grade or better and were used as received. All solvents were dried by routine techniques under an inert argon atmosphere.[27] Unless otherwise stated, manipulations of Mn^{II} complexes were carried out under argon using a glovebox or Schlenck techniques.

Instrumentation. ^{1}H NMR spectra were obtained on a Bruker DRX 400 MHz NMR spectrometer. Electronic absorption spectra were recorded on a Cary 50 Bio spectrophotometer (Varian) interfaced with a Unisoku cryostat (USP-203-A). Mass spectrometry experiments were performed using an LCT Primers MicroMass electrospray-ionization time-of-flight instrument. Magnetic circular dichroism (MCD) spectra were collected on a spectropolarimeter (Jasco J-815) interfaced with a magnetocryostat (Oxford Intruments SM-4000-8) capable of horizontal fields up to 8 T. Solution magnetic moments of $[Mn(L^7py_2^R)](ClO_4)_2$ complexes were determined by the ^{1}H NMR method of Evans in CD_3CN at 298 K.[28]

Ligand Synthesis. 1,4-Bis(2-pyridylmethyl)-1,4-diazepane ($L^7py_2^H$) and 1,4-bis(6-methyl-2-pyridylmethyl)-1,4-diazepane ($L^7py_2^{Me}$) were prepared by a previously reported reductive amination procedure, where homopiperazine is reacted with 2-pyridinecarboxaldehyde and 6-methyl-2-pyridinecarboxaldehyde, respectively.[29] The ligands 1,4-bis(5-bromo-2-pyridylmethyl)-1,4-diazepane ($L^7py_2^{Br}$) and 1,4-bis(6-methoxy-2-pyridylmethyl)-1,4-diazepane ($L^7py_2^{MeO}$) were prepared following the same procedure using 5-bromo-2-pyridinecarboxaldehyde and 6-methoxy-2-pyridinecarboxaldehyde, respectively. ^{1}H NMR data (400 MHz) for $L^7py_2^{Br}$ and $L^7py_2^{MeO}$ are as follows: $L^7py_2^{Br}$ ($CDCl_3$; δ) = 8.61 (s, 2H), 7.80 (d, 2H, J_{HH} = 20.12), 7.42 (d, 2H, J_{HH} = 8.28), 3.78 (s, 4H), 2.79 (m, 8H), 1.84 (m, 2H); $L^7py_2^{MeO}$ ($CDCl_3$; δ) = 7.55 (m, 2H), 7.04 (d, 2H, J_{HH} = 7.16), 6.60 (d, 2H, J_{HH} = 8.16), 3.93 (s, 6H), 3.77 (s, 4H), 2.84 (m, 8H), 1.87 (m, 2H).

Preparation of $[Mn(L^7py_2^R)](ClO_4)_2$ Complexes. $[Mn(L^7py_2^R)](ClO_4)_2$ complexes were synthesized in excellent yields (~85%) by reacting $L^7py_2^R$ (R = H, Br, Me, MeO) ligands with $Mn(ClO_4)_2$ in acetonitrile (MeCN) solution in a 1:1 molar ratio. Details of a representative preparation are as follows. To a stirred solution of 82 mg (0.323 mmol) of $Mn(ClO_4)_2$ in 10 mL of MeCN was added $L^7py_2^{Me}$ (100 mg, 0.322 mmol) in 10 mL of MeCN. The yellow solution was stirred overnight and evaporated under reduced pressure, and the solid thus obtained was dried in vacuo. Recrystallization of the crude solid from MeCN/diethyl ether afforded 155 mg (85%) of $[Mn(L^7py_2^{Me})](ClO_4)_2$ as nearly colorless crystals. Electrospray ionization mass spectrometry (ESI-MS) was used to explore the liquid-state composition of the purified $[Mn(L^7py_2^R)](ClO_4)_2$ complexes in MeCN solution. ESI-MS data are as follows: $\{[Mn(L^7py_2^H)](ClO_4)^+\}$ m/z = 436.0707 (calcd 436.0710), $\{[Mn(L^7py_2^{Br})](ClO_4)^+\}$ m/z = 593.8927 (calcd 593.8900), $\{[Mn(L^7py_2^{Me})](ClO_4)_2^+\}$ m/z = 464.1023 (calcd 464.1023), $\{[Mn(L^7py_2^{MeO})](ClO_4)_2^+\}$ m/z = 496.0899 (calcd 496.0921). *Caution! While no problems were encountered during this work, care should always be taken when handling perchlorate salts of metal complexes because of the possibility of explosion.*

X-ray Crystallography. Single crystals of $[Mn(L^7py_2^{Me})(CH_3CN)(ClO_4)](ClO_4)$ and $[Mn(L^7py_2^{MeO})(ClO_4)_2]$ were grown by vapor diffusion of ether into MeCN solutions of the complexes at room temperature. Single crystals of $[Mn(L^7py_2^H)(CH_3CN)_3](ClO_4)_2$ were grown by a similar vapor-diffusion method at −20 °C. Single crystals of $[Mn(L^7py_2^{Br})(OCMe_2)(ClO_4)](ClO_4)$ were grown by vapor diffusion of ether into an acetone solution of the complex at room temperature. Data collection and refinement parameters are summarized in Tables S1−S4.

For each sample, a full hemisphere of diffracted intensities was measured for a single-domain specimen using graphite-monochromated Mo Kα radiation (λ = 0.710 73 Å) on a Bruker SMART APEX CCD Single Crystal Diffraction System.[30] X-rays were provided by a fine-focus sealed X-ray tube operated at 45 kV and 35 mA. Lattice constants were determined with the Bruker SAINT software package. The Bruker software package SHELXTL was used to solve the structure using "direct methods" techniques. All stages of weighted full-matrix least-squares refinement were conducted using F_o^2 data with the SHELXTL Version 6.10 software package.[31] Experimental descriptions of XRD data collection and analysis for specific samples are included in the Supporting Information.

In Situ Preparation of Peroxomanganese(III) Complexes. The green peroxomanganese(III) intermediates $[Mn^{III}(O_2)(L^7py_2^R)]^+$ (R = H, Me, Br, and MeO) were formed by treating an acetonitrile solution of $[Mn^{II}(L^7py_2^R)](ClO_4)_2$ with 5 equiv of H_2O_2 and 0.5 equiv of triethylamine at −40 °C. The formation of the $[Mn^{III}(O_2)(L^7py_2^R)]^+$ complexes was evident from the appearance of characteristic bands in the electronic absorption spectra and supported by ESI-MS data (*vide infra*). These intermediates could also be prepared using KO_2 as the oxidant. For these reactions, a stock solution of KO_2 was made by dissolving 1:5 KO_2/18-Crown-6 (mol/mol) in acetonitrile. Treatment of an acetonitrile solution of $[Mn^{II}(L^7py_2^R)](ClO_4)_2$ with 1 equiv of KO_2/18-Crown-6 at −40 °C resulted in the formation of the $[Mn^{III}(O_2)(L^7py_2^R)]^+$ complexes.

Magnetic Circular Dichroism Experiments. 10 mM frozen glass samples of $[Mn^{III}(O_2)(L^7py_2^H)]^+$ and $[Mn^{III}(O_2)(L^7py_2^{Me})]^+$ were prepared in butyronitrile at −40 °C. Butyronitrile was used instead of MeCN, as the former produces an optical-quality glass upon freezing. We concluded that the solvent switch did not affect the composition of $[Mn^{III}(O_2)(L^7py_2^H)]^+$, as absorption spectra of $[Mn^{III}(O_2)(L^7py_2^H)]^+$ in MeCN and butyronitrile are virtually identical. Once formation of the peroxomanganese(III) species was complete (as monitored by UV−visible spectroscopy), the samples were cooled to −80 °C, transferred to precooled MCD cells, and flash-frozen in liquid N_2. To assess sample purity, ESI-MS

(27) Armarego, W.; Chai, C. *Purifications of Laboratory Chemicals*, 5th ed.; Elsevier: Burlington, MA, 2003.
(28) Evans, D. F.; Jakubovic, D. A. *J. Chem. Soc., Dalton Trans.* **1988**, 2927–2933.
(29) Mayilmurugan, R.; Stoeckli-Evans, H.; Palaniandavar, M. *Inorg. Chem.* **2008**, *47*, 6645–6658.
(30) *Data Collection: SMART Software Reference Manual*. Bruker-AXS. 5465 E. Cheryl Parkway, Madison, WI 53711-5373 USA, 1998.
(31) Sheldrick, G. M. Bruker-AXS, 5465 E. Cheryl Parkway, Madison, WI 53711-5373 USA, 2000.

experiments were performed on the remainder of the solution sample. The obtained MCD spectra were measured in mdeg (θ) and converted to $\Delta\epsilon$ (M^{-1} cm^{-1}) using the standard conversion factor $\Delta\epsilon = \theta/(32980 \cdot c \cdot d)$, where c is the concentration of the sample and d is the path length. MCD spectra were collected at 2, 4, 8, and 15 K for positive and negative field strengths of 1 to 7 T in 1 T increments. VTVH data were fit using the general method developed by Neese and Solomon.[32] Fits were performed for an $S = 2$ system with isotropic g-values of 2.00. Using a previously described protocol,[33] zero-field splitting (ZFS) parameters D and E/D were systematically varied while the transition moment products were optimized for a given set of ZFS parameters.

Density Functional Theory Computations. The *ORCA* 2.7 software package was used for all DFT computations.[34] Initial models of $[Mn^{III}(O_2)(L^7py_2^R)]^+$ (R = H and Me) were built using the X-ray coordinates of the corresponding manganese(II) complexes and adding side-on peroxo ligands. Geometry optimizations for models of $[Mn^{III}(O_2)(L^7py_2^R)]^+$ complexes were converged to the $S = 2$ spin and employed the Becke−Perdew (BP86) functional[35,36] and the SV(P) (Ahlrichs split valence polarized) basis with the SV/C auxiliary basis for all atoms except for manganese, nitrogen, and oxygen, where the larger TZVP (Ahlrichs triple-ζ valence polarized) basis in conjunction with the TZV/J auxiliary basis were used.[37,38] These calculations employed the resolution of identity (RI) approximation developed by Neese.[39] Solvation effects associated with acetonitrile (dielectric constant $\epsilon = 36.6$) were incorporated using COSMO, as implemented in *ORCA*.[40] The propyl and ethyl linkers in the diazacycloalkane fragment of the $L^7py_2^R$ ligands create two different faces when this ligand is bound in a *trans* geometry, as observed for the Mn^{II} complexes (*vide infra*). Therefore, in constructing our computational models of $[Mn^{III}(O_2)(L^7py_2^R)]^+$, we considered two isomers for the simplest $[Mn^{III}(O_2)(L^7py_2^H)]^+$ complex, where the peroxo ligand is adjacent to either the propyl (**P**) or ethyl (**E**) linkers (see Figure S1). The **P** isomer is predicted to be lower energy than the **E** isomer by only ~1 kcal/mol, which is well within the error expected for DFT calculations.[41] In addition, the TD-DFT computed absorption spectra of isomers **P** and **E** are essentially identical, indicating that these nearly isoenergetic isomers are expected to display very similar optical properties. Accordingly, we only considered isomer **P** in our analysis, under the assumption that, while there may likely be two isomers present in experimental samples of $[Mn^{III}(O_2)(L^7py_2^H)]^+$, these isomers will have virtually identical geometric and electronic structures. The coordinates of all DFT energy-minimized models presented in this study are included as Supporting Information (Tables S6−S8).

Electronic transition energies and intensities were computed for $[Mn^{III}(O_2)(L^7py_2^H)]^+$ and $[Mn^{III}(O_2)(L^7py_2^{Me})]^+$ using the time-dependent (TD)-DFT method[42−44] within the Tamm−Dancoff approximation.[45,46] These calculations employed the B3LYP functional[47−49] and TZVP (Mn, N, and O) and SVP (C and H) basis sets. In each calculation, 40 excited states were calculated by including all one-electron excitations within an energy window of ±3 hartree with respect to the HOMO/LUMO energies. Isosurface plots of molecular orbitals and electron density difference maps (EDDMs) were generated using the gOpenMol program using isodensity values of 0.05 and 0.02 b^{-3}, respectively.

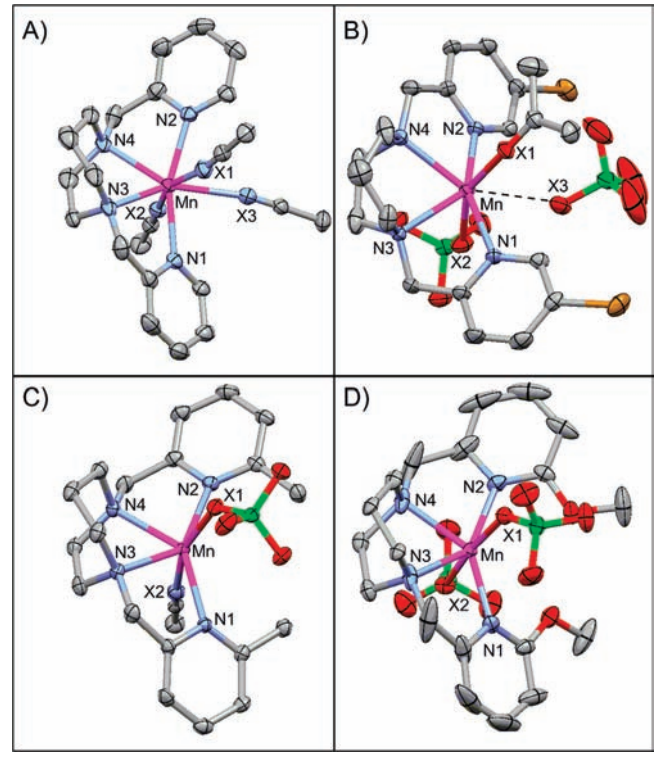

Figure 2. ORTEP diagrams of (A) $[Mn^{II}(L^7py_2^H)(NCMe)_3](ClO_4)_2$ (**1-H**), (B) $[Mn^{II}(L^7py_2^{Br})(OCMe_2)(ClO_4)](ClO_4)$ (**1-Br**), (C) $[Mn^{II}(L^7py_2^{Me})(NCMe)(ClO_4)](ClO_4)$ (**1-Me**), and (D) $[Mn^{II}(L^7py_2^{MeO})(ClO_4)_2]$ (**1-MeO**) showing 50% probability thermal ellipsoids. Hydrogen atoms and noncoordinating perchlorate counteranions have been removed for clarity. Significant interatomic distances and angles are listed in Table 1.

Results and Discussion

Structures and Physical Properties of $[Mn^{II}(L^7py_2^R)](ClO_4)_2$ Complexes. Figure 2 displays ORTEP diagrams for the four manganese(II) complexes $[Mn^{II}(L^7py_2^H)(NCMe)_3](ClO_4)_2$ (**1-H**), $[Mn^{II}(L^7py_2^{Br})(OCMe_2)(ClO_4)](ClO_4)$ (**1-Br**), $[Mn^{II}(L^7py_2^{Me})(NCMe)(ClO_4)](ClO_4)$ (**1-Me**), and $[Mn^{II}(L^7py_2^{MeO})(ClO_4)_2]$ (**1-MeO**). Selected bond distances and angles are given in Table 1. The amine nitrogens (N3 and N4; see Figure 2) of the **1-H** and **1-Br** complexes are seen to be linked by a high-occupancy (~80%) pair of ethylene and propylene chains and a pair of low-occupancy (~20%) chains, consistent with cocrystallization of two different conformations of the metal complex that have virtually identical sizes and shapes. Metric parameters for the high-occupancy species are displayed in Table 1, whereas corresponding parameters for the low-occupancy species are included in the Supporting Information. Importantly, the metric parameters among these complexes are comparable. For the

(32) Neese, F.; Solomon, E. I. *Inorg. Chem.* **1999**, *38*, 1847–1865.
(33) Jackson, T. A.; Karapetian, A.; Miller, A.-F.; Brunold, T. C. *Biochemistry* **2005**, *44*, 1504–1520.
(34) Neese, F. *ORCA - an ab initio, Density Functional and Semiempirical Program Package*, version 2.7; University of Bonn, 2009.
(35) Becke, A. D. *J. Chem. Phys.* **1986**, *84*, 4524–4529.
(36) Perdew, J. P. *Phys. Rev. B* **1986**, *33*, 8822–8824.
(37) Schäfer, A.; Horn, H.; Ahlrichs, R. *J. Chem. Phys.* **1992**, *97*, 2571–2577.
(38) Schäfer, G.; Huber, C.; Ahlrichs, R. *J. Chem. Phys.* **1994**, *100*, 5829–5835.
(39) Neese, F. *J. Comput. Chem.* **2003**, *24*, 1740–1747.
(40) Sinnecker, S.; Rajendran, A.; Klamt, A.; Diedenhofen, M.; Neese, F. *J. Phys. Chem. A* **2006**, *110*, 2235–2245.
(41) Siegbahn, P. E. M. *J. Biol. Inorg. Chem.* **2006**, *11*, 695–701.
(42) Bauernschmitt, R.; Ahlrichs, R. *Chem. Phys. Lett.* **1996**, *256*, 454–464.
(43) Casida, E. M.; Jamorski, C.; Casida, K. C.; Salahub, D. R. *J. Chem. Phys.* **1998**, *108*, 4439–4449.
(44) Stratman, R. E.; Scuseria, G. E.; Frisch, M. J. *J. Chem. Phys.* **1998**, *109*, 8218–8224.
(45) Hirata, S.; Head-Gordon, M. *Chem. Phys. Lett.* **1999**, *302*, 375–382.
(46) Hirata, S.; Head-Gordon, M. *Chem. Phys. Lett.* **1999**, *314*, 291–299.
(47) Becke, A. D. *J. Chem. Phys.* **1993**, *98*, 1372–1377.
(48) Becke, A. D. *J. Chem. Phys.* **1993**, *98*, 5648–5652.
(49) Lee, C.; Yang, W.; Parr, R. G. *Phys. Rev. B* **1988**, *37*, 785–789.

Table 1. Selected Bond Lengths (Å) and Angles (deg) for Complexes **1-H**, **1-Br**, **1-Me**, and **1-MeO**

Complex **1-H**			
Mn−N(1)	2.306(3)	N(1)−Mn−N(2)	158.8(1)
Mn−N(2)	2.308(2)	N(1)−Mn−N(3)	72.0(1)
Mn−N(3)	2.369(3)	N(2)−Mn−N(4)	71.4(1)
Mn−N(4)	2.357(2)	N(3)−Mn−N(4)	67.4(1)
Mn−X(1)	2.268(2)	X(1)−Mn−X(2)	160.0(1)
Mn−X(2)	2.311(2)	X(1)−Mn−X(3)	79.5(1)
Mn−X(3)	2.478(2)	X(2)−Mn−X(3)	80.8(1)
Complex 1-Br			
Mn−N(1)	2.262(3)	N(1)−Mn−N(2)	154.1(1)
Mn−N(2)	2.285(3)	N(1)−Mn−N(3)	73.6(1)
Mn−N(3)	2.323(4)	N(2)−Mn−N(4)	71.2(1)
Mn−N(4)	2.341(3)	N(3)−Mn−N(4)	68.9(1)
Mn−X(1)	2.200(2)	X(1)−Mn−X(2)	154.2(1)
Mn−X(2)	2.292(2)	X(1)−Mn−X(3)	80.8(1)
Mn···X(3)	2.679(3)	X(2)−Mn−X(3)	74.1(1)
Complex 1-Me			
Mn−N(1)	2.284(2)	N(1)−Mn−N(2)	143.34(7)
Mn−N(2)	2.284(2)	N(1)−Mn−N(3)	76.32(7)
Mn−N(3)	2.306(2)	N(2)−Mn−N(4)	75.02(7)
Mn−N(4)	2.285(2)	N(3)−Mn−N(4)	69.50(7)
Mn−X(1)	2.212(2)	X(1)−Mn−X(2)	161.91(7)
Mn−X(2)	2.280(2)		
Complex 1-MeO			
Mn−N(1)/N(2)	2.176(2)	N(1)−Mn−N(2)	142.1(1)
Mn−N(3)/N(4)	2.308(2)	N(1)−Mn−N(3)	75.7(1)
Mn−X(1)/X(2)	2.278(2)	N(3)−Mn−N(4)	70.3(1)
		X(1)−Mn−X(2)	173.1(1)

1-MeO complex, the Mn atom lies along a crystallographic C_2 axis, and thus the respective pyridine nitrogens, amine nitrogens, and perchlorate groups are symmetry related (Table 1).

For each of the four **1-R** complexes shown in Figure 2, the linear, tetradentate $L^7py_2^R$ ligand is bound in the *trans* configuration, as opposed to the *cis*-α or *cis*-*β* isomers. This observed configuration creates two *trans* coordination sites occupied by solvent and/or perchlorate ligands (X1 and X2; see Figure 2). In the cases of **1-H** and **1-Br**, a seventh ligand is bound in the equatorial plane and flanked by the pyridine rings of the $L^7py_2^H$ and $L^7py_2^{Br}$ ligands. For all complexes, the Mn^{II}−ligand bond lengths range from ∼2.1 to 2.5 Å, expected distances for high-spin Mn(II) centers.

Differences in the crystallographic structures of these Mn^{II} complexes can be attributed to the distinct steric and electronic influences caused by the pyridine substituents. Manganese(II) complexes can exist in a variety of geometries, including six-, seven-, and eight-coordinate forms.[50,51] The **1-H** complex containing the sterically unencumbered $L^7py_2^H$ ligand displays a seven-coordinate manganese(II) ion in a distorted pentagonal bipyramidal geometry. The tetradentate $L^7py_2^H$ ligand defines the equatorial plane, though this plane is quite ruffled; the mean deviation of the nitrogen atoms from this plane is 0.747 Å. The seven coordinate structure is completed by three MeCN solvent molecules occupying a meridional plane. The equatorial acetonitrile ligand (labeled X3 in Figure 2) displays a weak interaction with the Mn^{II} center (Mn^{II}−NCMe distance of 2.479 Å), and the Mn−NCMe vector roughly bisects the two $Mn-N_{amine}$ bonds. The Mn^{II} center of the **1-Br** complex is likewise seven-coordinate, with a weakly associated perchlorate anion in the equatorial plane ($Mn-OClO_3$ distance of 2.679 Å). Because this complex was crystallized in acetone/ether, an axially bound acetone ligand is observed rather than an MeCN ligand.

Scheme 2

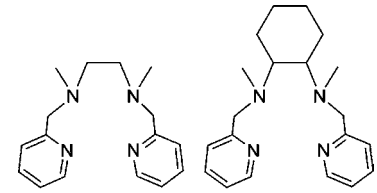

Unlike **1-H** and **1-Br**, the **1-Me** and **1-MeO** complexes are six-coordinate in the solid state structures (Figure 2), which is likely due to both electronic and steric effects. This reduced coordination number could be attributed to the greater electron-donating abilities of the methyl- and methoxy-appended pyridine ligands, as these electron-donating functionalities will reduce the Lewis acidity of the Mn^{II} center and could be expected to support a complex with a lower coordination number when compared with complexes supported by the $L^7py_2^H$ and $L^7py_2^{Br}$ ligands. In support, it was recently reported that the coordination number of Mn^{III} Schiff base complexes can be controlled by the presence or absence of electron-withdrawing $-CF_3$ groups on the ligand.[52] Specifically, six-coordinate Mn^{III} complexes were observed in complexes with $-CF_3$ groups, whereas five-coordinate complexes were evident when these groups were absent. For **1-Me** and **1-MeO**, the steric bulk of the methyl and methoxy substituents would additionally be expected to block the binding of a seventh ligand between the two pyridine rings (see Figure S2 for a comparison of the space filling diagrams of the **1-R** complexes). It is quite likely that both steric and electronic effects contribute to the lower coordination number of the **1-Me** and **1-MeO** complexes.

The solution structures of these manganese(II) salts were probed using electrospray ionization mass spectrometry (ESI-MS) and magnetic experiments. In all ESI-MS experiments, prominent ion peaks corresponding to a cationic mononuclear species, specifically, $\{Mn^{II}(L^7py_2^R)(ClO_4)\}^+$ ions, were observed at m/z = 436.0707 (**1-H**), 593.8927 (**1-Br**), 464.1023 (**1-Me**), and 496.0899 (**1-MeO**). In addition, the spin states of the manganese(II) complexes in deuterated MeCN solution were probed using the ^{1}H NMR method of Evans.[28] Analysis of the ^{1}H NMR data revealed room-temperature effective magnetic moments of ∼5.80−6.1 μ_B (Table S9), consistent with theoretical values expected for high-spin manganese(II) systems (μ_{eff} = 5.92 μ_B).

It is informative to discuss the structures of these Mn(II) complexes within the context of previously reported structures that feature other linear, tetradentate ligands (Scheme 2), such as BPMEN (BPMEN = *N*,*N*′-dimethyl-*N*,*N*′-bis(2-pyridylmethyl)-1,2-ethane diamine) and BPMCN (BPMCN = *N*,*N*′-dimethyl-*N*,*N*′-bis(2-pyridylmethyl)-1,2-cyclohexanediamine). The $[Mn^{II}(BPMEN)Cl_2]$ and $[Mn^{II}(R,R\text{-BPMCN})(CF_3SO_3)_2]$ complexes both display the ligands bound in the *cis*-α

(50) Ghachtouli, S. E.; Mohamadou, A.; Barbier, J.-P. *Inorg. Chim. Acta* **2005**, *358*, 3873–3880.
(51) Wang, S.; Westmoreland, D. *Inorg. Chem.* **2008**, *48*, 719–727.
(52) Darensbourg, D. J.; Frantz, E. B. *Inorg. Chem.* **2008**, *47*, 4977–4987.

conformation,[53,54] with the respective chloride and triflate anions *cis* to one another and *trans* to the amine nitrogens. The presence of these *cis* labile binding sites has been proposed to be important for catalytic epoxidation reactions involving peracetic acid as the terminal oxidant.[54,55] Presumably, these *cis* labile sites also contribute to the facile formation of bis(μ-oxo)-bridged dimers for the Mn_2(III,III), Mn_2(III,IV), and Mn_2(IV,IV) forms of these complexes.[53,56−61] In contrast, the *trans* orientations observed for the **1-R** complexes with the pyridyl-appended diazacycloalkane $L^7py_2^R$ ligands (Figure 2) are consistent with the observations of Que and Halfen, who reported the $L^7py_2^H$ ligand bound in a *trans* fashion for Cu^{II} and Fe^{II} complexes.[62−64] An exception to these observations is the recent report of iron(III) complexes of the $L^7py_2^H$ ligand bound in the *cis*-β orientation.[29] We attribute this difference to the fact that this complex was cocrystallized with a bidentate tetrachlorocatecholate ligand, which, because of its structural rigidity, cannot bind in a bidentate fashion if the $L^7py_2^H$ ligand is in a *trans*-conformation. Thus, while the $L^7py_2^R$ ligands are flexible in their binding modes, the *trans*-conformation appears to be preferred, in contrast to that reported for the similar BPMEN and BPMCN ligands.

Characterization of $[Mn^{III}(O_2)(L^7py_2^R)]^+$ Intermediates. The absorption spectra of acetonitrile solutions of all **1-R** complexes are featureless at wavelengths above 300 nm. This is expected, as the $d-d$ transitions for these high-spin Mn^{II} centers are all spin-forbidden, and no charge transfer (CT) transitions involving the pyridine and amine ligands are anticipated in the visible region. When 5 equiv of H_2O_2 and 0.5 equiv of triethylamine are added to a 2.5 mM solution of $[Mn^{II}(L^7py_2^H)]^{2+}$ in MeCN at −40 °C, a forest green intermediate (**2-H**) is formed. The absorption spectrum of **2-H** is characterized by a prominent absorption band at 445 nm and a weaker, broader band at 590 nm (ε = 280 and 120 M^{-1} cm^{-1}, respectively, Figure 3, top). The formation of these absorption bands upon addition of H_2O_2 is consistent with oxidation of the Mn^{II} ion, as complexes with higher oxidation state Mn centers (i.e., Mn^{III} and Mn^{IV}) commonly display absorption bands in the visible region. While **2-H** is stable at −40 °C for several hours, the $t_{1/2}$ at 0 °C is approximately 15 min. Due to this thermal instability, we have not been able to prepare crystals of **2-H** suitable for XRD experiments. Accordingly, we used ESI-MS to aid in defining the molecular composition of **2-H**. The ESI-MS spectrum of **2-H** exhibits a prominent ion peak at m/z = 369.1121, whose

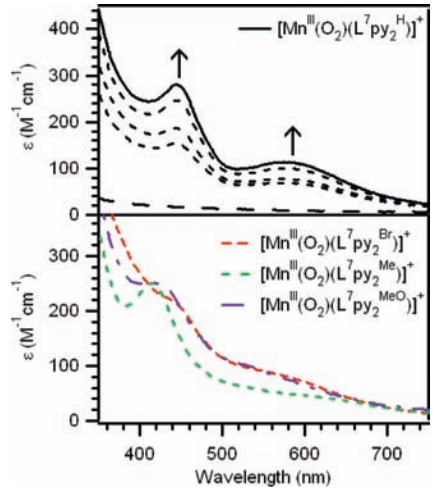

Figure 3. Top: Formation of $[Mn^{III}(O_2)(L^7py_2^H)]^+$ following the addition of 5 equiv H_2O_2 and 0.5 equiv of triethylamine to $[Mn^{II}(L^7py_2^H)]^{2+}$ in MeCN at −40 °C. Bottom: Electronic absorption spectra of $[Mn^{III}(O_2)(L^7py_2^{Br})]^+$, $[Mn^{III}(O_2)(L^7py_2^{Me})]^+$, and $[Mn^{III}(O_2)(L^7py_2^{MeO})]^+$ at −40 °C in MeCN.

Scheme 3

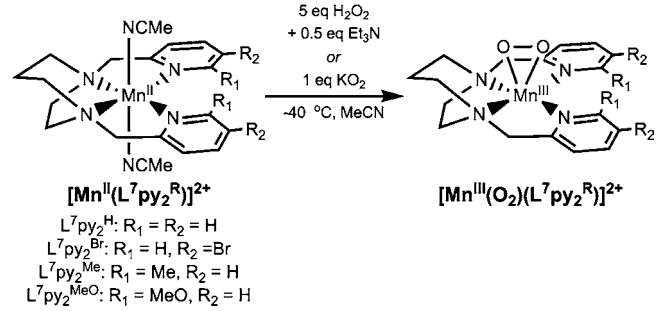

mass and isotope pattern corresponds to the $[Mn^{III}(O_2)(L^7py_2^H)]^+$ cation (calculated 369.1123) (Figure S3). When **2-H** is generated with isotopically labeled $H_2{}^{18}O_2$, the major ion peak upshifts by four mass units to m/z = 373.1157, indicating that the oxygen atoms of **2-H** derive from hydrogen peroxide. An alternative route for forming **2-H** was achieved by treating the corresponding Mn^{II} complex with 1 equiv of KO_2 in the presence of 18-Crown-6 in MeCN at −40 °C. Identical absorption and ESI-MS data are obtained regardless of whether H_2O_2/Et_3N or KO_2 are used to form **2-H**. This latter route has the advantage that H_2O and base are not introduced into the reaction mixture.

The absorption spectrum of **2-H** (Figure 3, top) bears a striking resemblance to that reported for the crystallographically characterized complex $[Mn^{III}(O_2)(TMC)]^+$, which displayed an intense absorption band at 453 nm with a broader band at 630 nm (ε = 490 and 120 M^{-1} cm^{-1}, respectively).[20] The spectral similarities between these complexes, along with our ESI-MS data for **2-H**, lead us to conclude that **2-H** likewise contains a six-coordinate Mn^{III} center with a peroxo ligand bound in a side-on η^2 fashion (Scheme 3). Further confirmation for the Mn^{III} oxidation state is provided by VTVH MCD data described in the following section. The observation that peroxomanganese(III) complex **2-H** can be formed using either H_2O_2 or KO_2 as the oxidant parallels that reported for $[Mn^{III}(O_2)(Me\text{-}TPEN)]^+$.[16,17] The observed reactivity of **1-H** with H_2O_2 is in contrast to that observed when Mn^{II} salts of BPMEN and BPMCN are treated with H_2O_2, as oxo-bridged dimers were

(53) Hureau, C.; Blondin, G.; Charlot, M.-F.; Philouze, C.; Nierlich, M.; Cesario, M.; Anxolabéhère -Mallart, E. *Inorg. Chem.* **2005**, *44*, 3669–3683.
(54) Murphy, A.; Dubois, G.; Stack, T. D. P. *J. Am. Chem. Soc.* **2003**, *125*, 5250–5251.
(55) Murphy, A.; Stack, T. D. P. *J. Mol. Catal. A: Chem.* **2006**, *251*, 78–88.
(56) Glerup, J.; Goodson, P. A.; Hazell, A.; Hazell, R.; Hodgson, D. J.; McKenzie, C. J.; Michelsen, K.; Rychlewska, U.; Toftlund, H. *Inorg. Chem.* **2002**, *33*, 4105–4111.
(57) Goodson, P. A.; Glerup, J.; Hodgson, D. J.; Michelsen, K.; Pedersen, E. *Inorg. Chem.* **1990**, *29*, 503–508.
(58) Goodson, P. A.; Hodgson, D. J. *Inorg. Chem.* **1989**, *28*, 3606–3608.
(59) Goodson, P. A.; Glerup, J.; Hodgson, D. J.; Michelsen, K.; Weihe, H. *Inorg. Chem.* **1991**, *30*, 4909–4914.
(60) Goodson, P. A.; Oki, A. R.; Glerup, J.; Hodgson, D. J. *J. Am. Chem. Soc.* **1990**, *112*, 6248–6254.
(61) Collins, M. A.; Hodgson, D. J.; Michelsen, K.; Towle, D. K. *J. Chem. Soc., Chem. Commun.* **1987**, 1659–1660.
(62) Halfen, J. A.; Moore, H. L.; Fox, D. C. *Inorg. Chem.* **2002**, 41.
(63) Halfen, J. A.; Uhan, J. M.; Fox, D. C.; Mehn, M. P.; Que, L., Jr. *Inorg. Chem.* **2000**, *29*, 4913–4920.
(64) Chen, K.; Que, L. J. *Angew. Chem., Int. Ed.* **1999**, *38*, 2227–2229.

Table 2. Properties of Peroxomanganese(III) Complexes

	λ_{max} (nm) (ϵ (M^{-1} cm^{-1}))	$t_{1/2}$ at 0 °C	D (cm^{-1})	E/D
2-H	445 (280) 590 (120)	15 min	−2	0.13
2-Br	445 (220) 589 (90)	3 min	ND[a]	ND[a]
2-Me	415 (280) ~620 (80)	6 min	−3	0.05
2-MeO	416 (250) ~560 (80)	~seconds[b]	ND[a]	ND[a]

[a] Not determined. [b] This complex displays a $t_{1/2}$ of 6 min at −40 °C.

reported in those cases.[58,61,65] We attribute this difference in reactivity to the *trans* binding mode of the $L^7py_2^R$ ligands (Figure 2) that presumably disfavors dimerization.

When **1-Br**, **1-Me**, and **1-MeO** are treated either with H_2O_2 in the presence of base or with KO_2, new chromophoric species (**2-R**) are observed (Figure 3 and Table 2). While intermediate **2-Br** displays λ_{max} values virtually identical to those of **2-H**, both **2-Me** and **2-MeO** display a blue shift of the prominent absorption band to ~410 nm and a broadening of the lower-energy feature. In all cases these species are all less stable than **2-H** (Table 2). **2-Br** and **2-Me** display half-lives at 0 °C of 3 and 6 min, respectively. Intermediate **2-MeO** is significantly more unstable, exhibiting a half-life at −40 °C of 6 min. ESI-MS experiments performed for **2-Br** and **2-Me** reveal prominent ion peaks with *m*/*z* values consistent with cationic mononuclear $[Mn^{III}(O_2)(L^7py_2^R)]^+$ complexes (R = Br and Me) that all upshift by four *m*/*z* units when these samples are prepared with isotopically labeled $H_2{}^{18}O_2$. Owing to its instability, we were unable to obtain ESI-MS data for **2-MeO**, but on the basis of the similarities between the absorption spectra of **2-Me** and **2-MeO**, we likewise propose that **2-MeO** is a peroxomanganese(III) adduct.

Thus, by using the series of $L^7py_2^R$ ligands, we have prepared a set of four peroxomanganese(III) complexes that differ solely with regard to the identity of pyridine ring substituents. The differences in optical properties of these complexes, **2-H** and **2-Br** on the one hand, and **2-Me** and **2-MeO** on the other (Table 2), are indicative of structural and/or electronic perturbations caused by the different steric and electronic properties of the supporting ligand. To evaluate the origins of these perturbations in more detail, magnetic circular dichroism (MCD) spectroscopy was used to evaluate the excited- and ground-state properties of **2-H** and **2-Me**.

MCD and VTVH MCD Spectroscopy. Figure 4 shows the 233 K absorption and 4.5 K, 7 T MCD spectra of **2-H** plotted in wavenumbers (cm^{-1}). The two prominent absorption bands at ~16 000 and ~22 220 cm^{-1} (bands 1 and 2, respectively) correspond to positive features in the MCD spectrum, and an additional band at ~24 430 cm^{-1} (band 3) is also resolved. An iterative Gaussian deconvolution of the absorption and MCD data sets reveals a total of six electronic transitions from 14 000 to 30 000 cm^{-1} (Table S10). No additional features were observed down to 9000 cm^{-1} using either absorption or MCD spectroscopies. Given the low symmetry anticipated for **2-H**, four spin-allowed Mn^{III} $d-d$ bands are expected in the near-IR to near-UV region. Band 1 can be assigned as the lowest-energy $d-d$ transition, which for high-spin Mn^{III} complexes corresponds to an intra-e_g transition, using the symmetry labels from the parent octahedral point group. For strictly octahedral manganese(III) complexes, this band is typically observed at ~10 000 cm^{-1} and is a consequence of the Jahn−Teller splitting of the e_g orbitals.[66] Thus, the lowest energy $d-d$ band of **2-H** (band 1; Figure 4) is shifted to higher energy by ~6000 cm^{-1} relative to the majority of six-coordinate manganese(III) complexes, indicating an unusual electronic structure likely due to the presence of the peroxo ligand. Band 3 is assigned as the second Mn^{III} $d-d$ transition, as it is weak in the absorption spectrum but carries significant MCD intensity. Assignments for bands 2 and 4−6 are unclear given that none of these bands appear to be selectively enhanced in the MCD spectrum and, thus, are not able to be readily assigned as $d-d$ bands. Further complicating the assignment of these transitions is the fact that, on the basis of analogy with peroxoiron(III) systems, peroxo-to-manganese(III) charge-transfer (CT) transitions are anticipated in the visible region.[25,67] As discussed below, TD-DFT computations were performed to aid in assigning these transitions.

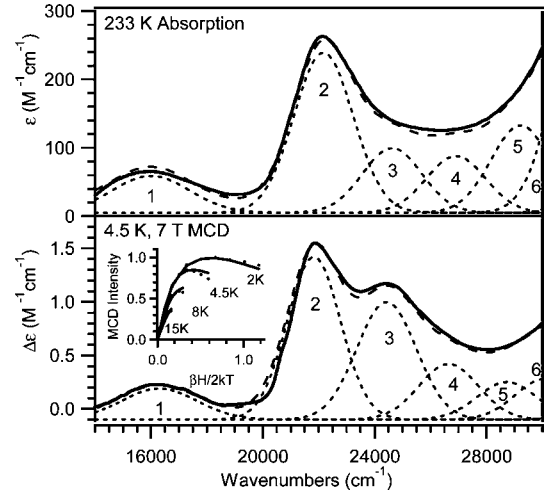

Figure 4. 233 K electronic absorption (top) and 4.5 K, 7 T MCD (bottom) spectra of $[Mn^{III}(O_2)(L^7py_2^H)]^+$ (**2-H**). Individual Gaussian curves (black dotted lines) and their sums (black dashed lines) obtained from iterative fits of these data sets are displayed on their respective spectra. Inset: Experimental VTVH MCD data collected at 21 872 cm^{-1} for 2-H (•••) and theoretical fit (−) using the following parameters: $D = -2.00$, $E/D = 0.130$, $g_{iso} = 2.00$, and 4% *x*, 5% *y*, and 91% *z* polarization. Conditions: Absorption data were collected for a 2.5 mM sample in CH_3CN. MCD data were collected for a 10 mM frozen glass sample in butyronitrile.

To assess the effects of changing the properties of the $L^7py_2^R$ ligand on the electronic structure, low-temperature MCD data were also collected for **2-Me** (Figure 5, bottom). Similar to the case observed for **2-H**, the major absorption bands of **2-Me** are retained in the MCD spectrum, but additional features are also apparent. Most notably, a lower energy band at ~13 500 cm^{-1} (band 1) is resolved, and bands 3 and 5 are significantly more prominent in the MCD spectrum (Figure 5). An iterative Gaussian deconvolution of the absorption and MCD spectra of **2-Me** reveals a total of seven transitions from 12 000 to 30 000 cm^{-1} (Table S11). Because of their relatively large MCD-to-absorption intensity ratios, bands 1, 3, and 5 are assigned as Mn^{III} $d-d$ bands. In contrast, bands 2, 4, and 6, which carry moderate absorption intensities, are comparatively weaker in the MCD spectrum, suggesting that these bands are charge transfer in origin. When compared to **2-H**, the most notable

(65) Glerup, J.; Goodson, P. A.; Hazell, A.; Hazell, R.; Hodgson, D. J.; McKenzie, C. J.; Michelsen, K.; Rychlewska, U.; Toftlund, H. *Inorg. Chem.* **1994**, *33*, 4105–4111.
(66) Lever, A. B. P. *Inorganic Electronic Spectroscopy*, 2nd ed.; Elsevier: Amsterdam; New York, 1984.
(67) Neese, F.; Solomon, E. I. *J. Am. Chem. Soc.* **1998**, *120*, 12829–12848.

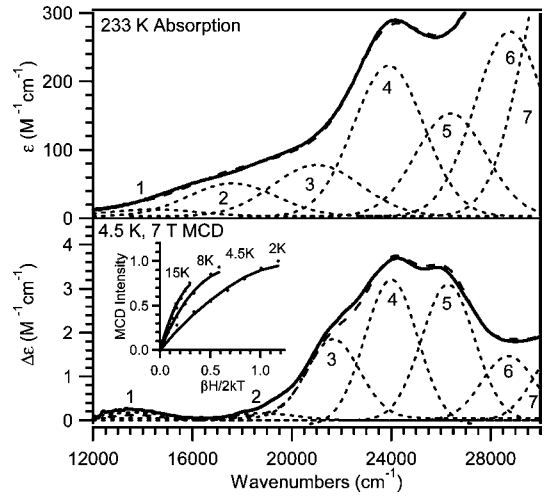

Figure 5. 233 K electronic absorption (top) and 4.5 K, 7 T MCD (bottom) spectra of $[Mn^{III}(O_2)(L^7py_2^{Me})]^+$ (**2-Me**). Individual Gaussian curves (black dotted lines) and their sums (black dashed lines) obtained from iterative fits of these data sets are displayed on their respective spectra. Inset: Experimental VTVH MCD data collected at 24 150 $cm^{-1}$for **2-Me** (•••) and theoretical fit (−) using the following parameters: $D = -3.00$, $E/D = 0.05$, $g_{iso} = 2.00$, and 0.001% *x*, 0.002% *y*, and 99.997% *z* polarization. Conditions: Absorption data were collected for a 2.5 mM sample in CH_3CN. MCD data were collected for a 10 mM frozen glass sample in butyronitrile.

difference for **2-Me** is the ∼2500 cm^{-1} red shift of the lowest-energy $d-d$ band (band 1). Importantly, this large shift is not evident from inspection of the corresponding absorption spectra. It is, however, readily appreciated when the MCD data sets are compared, illustrating the power of MCD spectroscopy to probe peroxomanganese(III) adducts.

While our analysis of the absorption and MCD spectra of **2-H** and **2-Me** provides transitions energies and intensities, it does not afford insight into the ground-state properties of these complexes. There are several powerful methods for probing the ground-state zero-field splitting parameters of transition metal centers, including inelastic neutron scattering[68] and multifrequency, high-field EPR spectroscopy.[69] Variable-temperature, variable-field (VTVH) MCD spectroscopy has also been shown to be an excellent tool for obtaining such parameters,[32,70] and we have therefore used it to examine the ground-state properties and transition polarizations of **2-H** and **2-Me**.

VTVH MCD curves obtained for **2-H** at 21 872 cm^{-1} (Figure 4; inset) are nested; i.e., higher temperature curves saturate more rapidly than lower temperature curves, indicating that the manganese(III) ion is subject to a moderate ZFS. Notably, the addition of a methyl group onto the L^7py_2 ligand framework significantly alters the VTVH saturation behavior of the MCD signal (cf. Figures 4 and 5; insets). Specifically, the VTVH MCD signals for **2-Me** saturate more slowly with increased field. Because neither transition polarizations nor ZFS parameters are known for **2-H** and **2-Me**, the VTVH MCD data sets for these species were systematically fit to extract these parameters. In this procedure, D and E/D were varied from −3 to 3 cm^{-1} and from 0 to 0.3 in increments of 0.5 and 0.05 cm^{-1}, respectively. Transition-moment products (*i.e.*, M_{xy}, M_{xz}, M_{yz}) were optimized to fit the experimental data for a given set of D and E/D values. The goodness of fit was assessed by the χ^2 value; where χ^2 is the sum of the squares of the differences between experimental and fit data sets. The best fits were obtained assuming an $S = 2$ spin state, further confirming our assignment of **2-H** and **2-Me** as high-spin Mn^{III} complexes. Excellent fits for **2-H** and **2-Me** ($\chi^2 < 0.12$) were obtained with D values of −2.0 and −3.0 cm^{-1} and E/D values of 0.13 and 0.05, respectively (Figures 4 and 5; insets). The observation that both complexes have axial ZFS parameters of the same sign (i.e., $D < 0$ cm^{-1}) implies that these species have similar orbital ground states. Because of the similarities in the D and E/D values, the transition polarizations were examined to understand the different nesting behavior of **2-H** and **2-Me**. Both transitions are highly *z*-polarized (>90%); however, the data for **2-H** and **2-Me** are best fit with 90% and 99% *z*-polarization, respectively. To explore whether this 9% change in polarization could account completely for the different nesting behaviors, we simulated VTVH MCD data for D and E/D values of −3.0 and 0.05, respectively, but with *z*-polarizations of 90 and 99%. It is evident from the resulting traces (Figure S4) that this small change in *z*-polarization can greatly affect the nesting behavior of these systems.

The ZFS parameters of **2-H** and **2-Me** (Table 2) are very similar to those previously reported for the peroxomanganese(III) complexes $[Mn^{III}(O_2)(Me\text{-}TPEN)]^+$ ($D = -2.9$ cm^{-1} and $E/D = 0.075$)[16,17] and $[Mn^{III}(O_2)(H_3bupa)]^-$ ($D = -2.0$ cm^{-1} and $E/D = 0.13$).[18] In each case the axial ZFS parameter D is negative, which is generally,[71] but not always,[72] a marker of a tetragonal elongation around the Mn^{III} center. For the $[Mn^{III}(O_2)(H_3bupa)]^-$ complex, it is actually unclear whether this species contains an η^2-$Mn^{III}-O_2$ or an η^1-$Mn^{III}-OOH$ adduct.[18] The strong similarity of the ZFS parameters of this complex with those of **2-H**, **2-Me**, and $[Mn^{III}(O_2)(Me\text{-}TPEN)]^+$ lends credence to the proposal that $[Mn^{III}(O_2)(H_3bupa)]^-$ contains an η^2-$Mn^{III}-O_2$ adduct. However, in the absence of corresponding data for a $Mn^{III}-OOH$ adduct, this should be viewed as a tentative conclusion.

Taken together, the results of the MCD and VTVH-MCD experiments for **2-H** and **2-Me** reveal that the ground- and excited-state properties of these complexes compare favorably, consistent with the similar structures expected for these peroxomanganese(III) complexes. Nonetheless, shifts in electronic transition energies indicate that the electronic structure of the $Mn^{III}-O_2$ unit is influence by the presence of pyridine ring substituents. To correlate these spectral shifts with changes in the geometric and electronic structure of the $Mn^{III}-O_2$ unit caused by ligand perturbations, density functional theory (DFT) and time-dependent DFT (TD-DFT) calculations were performed on models of **2-H** and **2-Me**.

DFT-Optimized Geometries. Important metric parameters of our DFT-optimized models of **2-H** and **2-Me** are collected in Table 3. In both cases, the optimized structures display six-coordinate Mn centers with side-on peroxo ligands, as shown for **2-H** in Figure 6. The nitrogen atoms of the supporting $L^7py_2^H$ ligand forms the base of a square plane that sits below the $Mn^{III}-O_2$ unit. Importantly, the computed O−O and Mn−O distances fall within the ranges observed for crystallographically

(68) Dobe, C.; Noble, C.; Carver, G.; Tregenna-Piggott, P. L. W.; McIntyre, G. J.; Barra, A.-L.; Neels, A.; Janssen, S.; Juranyi, F. *J. Am. Chem. Soc.* **2004**, *126*, 16639–16652.
(69) Krzystek, J.; Ozarowski, A.; Telser, J. *Coord. Chem. Rev.* **2006**, *250*, 2308–2324.
(70) Oganesyan, V. S.; George, S. J.; Cheesman, M. R.; Thomson, A. J. *J. Chem. Phys.* **1999**, *110*, 762–777.
(71) Scheifele, Q.; Riplinger, C.; Neese, F.; Weihe, H.; Barra, A.-L.; Juranyi, F.; Podlesnyak, A.; Tregenna-Piggott, P. L. W. *Inorg. Chem.* **2007**, *47*, 439–447.
(72) Mossin, S.; Weihe, H.; Barra, A. L. *J. Am. Chem. Soc.* **2002**, *124*, 8764.

Table 3. Metal−Ligand Bond Lengths (Å) for $[Mn^{III}(O_2)(L^7py_2^H)]^+$ and $[Mn^{III}(O_2)(L^7py_2^{Me})]^+$ Complexes Based on BP86 DFT Geometry Optimizations

	$[Mn^{III}(O_2)(L^7py_2^H)]^+$	$[Mn^{III}(O_2)(L^7py_2^{Me})]^+$
Mn−O^A	1.874	1.907
Mn−O^B	1.867	1.866
O^A−O^B	1.444	1.452
Mn−N1	2.215	2.296
Mn−N2	2.108	2.177
Mn−N3	2.212	2.147
Mn−N4	2.283	2.279

characterized peroxomanganese(III) complexes (the experimental distances are 1.40−1.43 Å and 1.84−1.90 Å, respectively).[19−22,24] However, while the model of **2-H** has relatively symmetric Mn−O bond lengths of 1.870 ± 0.005 Å, **2-Me** exhibits asymmetric Mn−O distances of 1.91 and 1.87 Å (Table 3). We attribute this to the great electron-donating ability of the $L^7py_2^{Me}$ ligand that reduces the Lewis acidity of the Mn^{III} center in **2-Me**. This observation is thus potentially related to the difference in coordination number observed for the corresponding Mn^{II} complexes, **1-H** and **1-Me**, that respectively displayed seven- and six-coordinate Mn^{II} centers (Figure 2). Notably, Nam and co-workers recently proposed that the presence of electron-donating ligands *trans* to the peroxo unit in Mn^{III}−O_2 species leads to more end-on-like peroxo ligands with asymmetric Mn−O bond lengths.[24] Our computations lend further credence to this proposal and additionally predict that *cis* ligands can have a similar effect.

The Mn *d* orbital splitting patterns of **2-H** and **2-Me** are shown in Figure 7. For these calculations, we have used a coordinate system with the *z*-axis perpendicular to the Mn^{III}−O_2 unit and the *x*-axis bisecting the O−O bond (see Figure 6). With this coordinate system, the Mn d_{xy} and d_{z^2} MOs are the σ-type orbitals (i.e., the e_g set), whereas the $d_{x^2-y^2}$, d_{xz}, and d_{yz} MOs are the π-type orbitals (i.e., the t_{2g} set). Using the commonly accepted hole formalism, the $(d_{yz})^1(d_{x^2-y^2})^1(d_{xz})^1(d_{z^2})^1(d_{xy})^0$ configurations predicted for both **2-H** and **2-Me** give rise to d_{xy} orbital ground states. The similar ground states predicted for these complexes are consistent with the observation that VTVH MCD data collected for **2-H** and **2-Me** are both best fit with $D < 0$ cm^{-1}.

Electronic Structure and Spectral Assignments for 2-H. Before comparing the electronic structures in detail, the bonding description afforded by DFT computations performed for **2-H** will be briefly summarized to provide a framework for understanding perturbations caused by the more side-on bound peroxo ligand in **2-Me**. The bonding in side-on peroxometal adducts is dominated by a σ-interaction involving the Mn d_{xy}

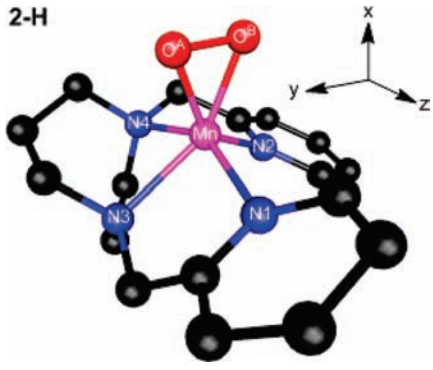

Figure 6. DFT-Optimized Model of $[Mn^{III}(O_2)(L^7py_2^H)]^+$ (**2-H**).

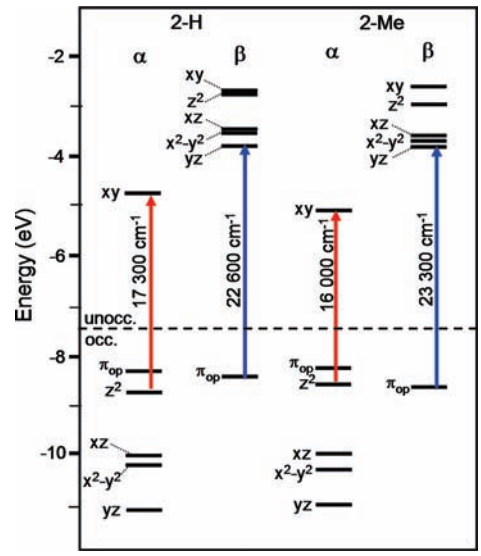

Figure 7. Molecular orbital (MO) energy-level diagrams for $[Mn^{III}(O_2)(L^7py_2^H)]^+$ (**2-H**; left) and $[Mn^{III}(O_2)(L^7py_2^{Me})]^+$ (**2-Me**; right) complexes obtained from spin-unrestricted DFT calculations. MOs are labeled according to their principal contributors. For clarity only Mn^{III} d-based and O_2 π_{op}*-based MOs are included. TD-DFT computed transition energies of prominent electronic transitions are also displayed.

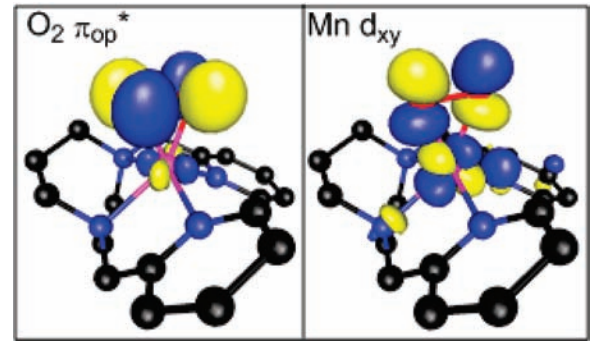

Figure 8. Surface contour plots of the spin-up O_2 π_{op}* (left) and Mn d_{xy} (right) MOs.

orbital and the in-plane peroxo π-antibonding orbital (π_{ip}*), as discussed previously for peroxoiron(III) complexes.[67] A plot of the Mn d_{xy} MO for **2-H** is shown in Figure 8 (right). The strength of the Mn−O_2 σ-interaction is evidenced by the relatively high percentage of peroxo character (∼48%) in this MO. We note that, because Mn^{III} is a d^4 ion, this Mn−O_{peroxo} σ-antibonding orbital is empty. This is in contrast to corresponding high-spin Fe^{III}−O_2 systems (d^5) where the related MO is half-filled. This difference in occupancy of the metal-peroxo σ-antibonding orbital could account for the fact that Fe^{III}−O_{peroxo} bond lengths in side-on peroxoiron(III) complexes[25] are, on average, longer than Mn^{III}−O_{peroxo} distances.[19−21,24]

In contrast to the high covalency of the Mn d_{xy} MO, the d_{z^2} MO of **2-H** carries only ∼5% peroxo character and is predominantly Mn-L^7py_2 σ-antibonding (Table S12). The t_{2g}-derived orbitals are involved in π-interactions with both the peroxo ligand and the π* orbitals of the pyridine rings of the $L^7py_2^H$ ligand. These π-interactions are rather weak and account for the small energy splitting observed for these MOs (Figure 7). Also included among the frontier orbitals of **2-H** are the filled out-of-plane peroxo π-antibonding orbital (π_{op}*). This is the highest-occupied MO for **2-H** and carries a small percentage of Mn d_{yz} character (Figure 8, left), representing a weak Mn−O_2

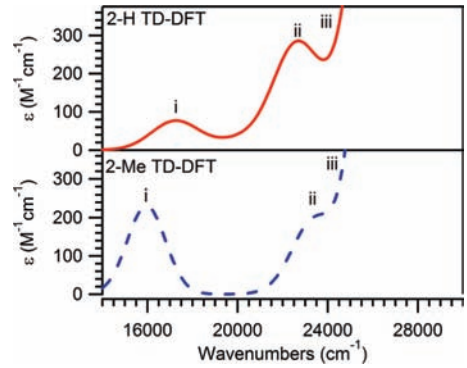

Figure 9. Simulated absorption spectra of $[Mn^{III}(O_2)(L^7py_2^H)]^+$ (**2-H**; top) and $[Mn^{III}(O_2)(L^7py_2^{Me})]^+$ (**2-Me**; bottom) based on TD-DFT computations employing the B3LYP functional.

π-interaction. To correlate this electronic structure description with the spectroscopic data collected for **2-H**, we next performed TD-DFT computations to predict electronic transition energies.

The TD-DFT computed absorption spectrum for **2-H** shown in Figure 9 (top) is strikingly similar to the experimental spectrum (Figure 4). A low-intensity band is predicted at 17 300 cm^{-1} (band *i*; Figure 9) that is in good agreement with the experimental feature at ~16 000 cm^{-1} (band 1; Figure 4). Band *i* is due solely to the Mn $d_{z^2} \rightarrow d_{xy}$ transition (Table S13), which is the lowest-energy $d-d$ transition. Because the acceptor orbital for this transition is the $Mn-O_2$ σ-antibonding MO, the relatively high energy of this transition compared to that of other six-coordinate Mn^{III} complexes can be attributed to the strong σ-covalency of the $Mn-O_{peroxo}$ bonds that destabilizes the d_{xy} MO. The higher-energy absorption band computed for **2-H** (band *ii*; Figure 9), which corresponds well with the experimental band at 22 200 cm^{-1} (band 2; Figure 4), is due to a weak peroxo-to-Mn^{III} charge transfer (CT) transition (O_2 $\pi_{op}^* \rightarrow$ Mn d_{yz}). The low intensity of this CT band (experimental $\epsilon \approx 500$ M^{-1} cm^{-1}) is due to the fact that the acceptor MO (Mn d_{yz}) has very little peroxo character. In addition to allowing us to assign the major features in the absorption spectrum of **2-H**, the TD-DFT calculations allow us to make assignments for additional bands resolved in the low-temperature MCD spectrum. Specifically band 3 (Figure 4) can be assigned as the second Mn $d-d$ transition ($d_{xz} \rightarrow d_{xy}$), which is predicted at ~24 600 cm^{-1}. This corroborates our initial assignment of band 3 as a $d-d$ transition based on its enhanced intensity in the MCD spectrum (Figure 4). At higher-energy, the TD-DFT calculations predict additional peroxo-to-Mn CT transitions as well as the remaining two $d-d$ bands (Table S13).

Electronic Structure and Spectral Assignments for 2-Me. The asymmetric $Mn-O_2$ bond lengths observed for **2-Me** attenuates the σ-interaction between the Mn d_{xy} and O_2 π_{ip}^* orbitals. This causes a reduction of the energy splitting between the spin-up d_{xy} and d_{z^2} MOs (Figure 7). Consequently, the $d_{z^2} \rightarrow d_{xy}$ transition is predicted at lower energy in the TD-DFT computed spectrum for **2-Me** (Figure 9), reproducing the experimentally observed red shift of this band when compared with **2-H**. The origin of this spectral shift is the more end-on binding mode of the peroxo ligand in **2-Me**. Further, these data suggest that there is a correlation between the energy of the $d_{z^2} \rightarrow d_{xy}$ transition and the Mn−O bond length.

The longer Mn−O bond lengths in **2-Me** are accompanied by a small elongation (0.01 Å) of the O−O distance compared with **2-H** (Table 3). This elongation stabilizes the spin-down O_2 π_{op}^* orbitals (Figure 7). As these are the donor orbitals for the prominent O_2 $\pi_{op}^* \rightarrow$ Mn d_{yz} transition, this stabilization causes a shift of this band to higher energy. To assess if this is a general trend, we systematically elongated the O−O bond for **2-H** and computed absorption spectra for these models. The results of these calculations show that lengthening the O−O bond leads to a steady blue shift of the O_2 $\pi_{op}^* \rightarrow$ Mn d_{yz} transition energy (Figure S5). Thus, the spectral perturbations of **2-Me** relative to **2-H** can both be explained by a more end-on binding mode of the peroxo ligand in the former complex that perturbs the energies of the Mn- and O_2-based MOs that are involved in the dominant electronic transitions.

Summary and Perspectives

A detailed understanding of the pathways by which biological and synthetic Mn centers activate dioxygen and hydrogen peroxide requires fundamental studies of potential intermediates involved in these processes. This paper describes the generation and characterization of a set of peroxomanganese(III) adducts supported by tetradentate $L^7py_2^R$ ligands with a range of steric and electronic properties. X-ray crystal structures of the corresponding Mn^{II} complexes indicate that in all cases the $L^7py_2^R$ ligands bind in the *trans* conformation. Importantly, this *trans* binding mode appears to favor the formation of mononuclear peroxomanganese(III) adducts over oxo-bridged dimers, at least at low temperature, as the latter species have been previously observed for similar ligand sets that coordinate Mn centers to give *cis*-α complexes.[58,61,65]

While it has been known for some time that the electronic absorption spectra of peroxomanganese(III) adducts are affected by the nature of the supporting ligand, the results reported herein offer evidence that these spectral signatures can be related to certain features of $Mn^{III}-O_2$ bonding. Specifically, we propose that the lowest-energy $d-d$ band should be a marker of the strength of the $Mn-O_{peroxo}$ σ-interaction, with lower-energy bands signifying weaker $Mn-O_{peroxo}$ bonds or peroxo ligands bound in a more end-on fashion. This correlation is possible because the acceptor orbital for this electronic transition is the $Mn-O_2$ σ-antibonding MO. Indeed, when the Mn−O distances of **2-H** are systematically varied from 1.82 to 1.88 Å, the TD-DFT-computed energy of the $d_{z^2} \rightarrow d_{xy}$ transition decreases from 18 200 to 17 000 cm^{-1} in a fairly linear fashion (Figure S6). Moreover, this model is consistent with the observation that $Mn^{III}-O_2$ complexes supported by the Tp^{iPr} ligand exhibit higher energy electronic transitions (~560 nm; 17 900 cm^{-1}) and shorter Mn−O bonds (~1.85 Å),[19,21] relative to the $[Mn(O_2)(TMC)]^+$ and $[Mn(O_2)(13\text{-}TMC)]^+$ complexes that respectively display lower energy bands at 630 and 615 nm (15 900 and 16 260 cm^{-1}) and longer Mn−O distances (1.884 and 1.859 Å).[20,24] In addition, this model lends credence to the proposal that the product-inhibited complex observed for MnSOD is essentially an end-on peroxomanganese(III) adduct with relatively long, asymmetric $Mn-O_{peroxo}$ bond lengths (1.80 and 2.22 Å), as this complex exhibits a low-energy absorption band at 650 nm (15 400 cm^{-1}).[33] One caveat of this proposal is that the $d_{z^2} \rightarrow d_{xy}$ transition energy will be modulated by interactions with the supporting ligand, as the donor orbital is the Mn-ligand σ^* MO. Further, we emphasize that, in some cases, the combined use of absorption and MCD spectroscopy will be required for identifying the lowest energy $d-d$ band, because $d-d$ bands are selectively enhanced in low-temperature MCD spectra. This is exemplified by **2-Me**, where the low energy band 1 is completely obscured in the electronic absorp-

tion spectrum but clearly evident in the low-temperature MCD spectrum (Figure 5).

Taken together, these results show that the electron-donating properties of supporting ligands are able to modulate the peroxo binding mode in $Mn^{III}-O_2$ complexes, with electron-rich ligands supporting more asymmetric $Mn-O_{peroxo}$ bonds. Thus, the use of electron-rich supporting ligands could provide a route to peroxo ligands primed for further activation.[24] The conditions under which a more complete conversion from a side-on to an end-on peroxo binding mode could occur are currently unclear. We do note, however, that the nearly end-on binding mode proposed for the peroxomanganese(III) adduct of MnSOD could offer insight into this issue, as the active site features a carboxylate ligand (aspartate) *trans* to the peroxo group.[33] To date, the only $Mn^{III}-O_2$ adduct featuring a carboxylate ligand is the $[Mn(O_2)(13\text{-TMC})(O_2CCF_3)]^+$ complex,[24] where the donating ability of the carboxylate function is significantly attenuated. Thus, the use of strongly electron-donating carboxylate functions might be required to foster $Mn^{III}-O_2$ adducts with more end-on geometries. In relation to nonheme iron systems, it is well established that side-on peroxoiron(III) centers are relatively unreactive, whereas end-on hydroperoxo- and alkylperoxoiron(III) complexes have been proposed to undergo O−O cleavage reactions to afford high-valent oxoiron intermediates.[25] Whether this reactivity pattern can be generally applied to manganese systems has yet to be determined.

Acknowledgment. The authors acknowledge the University of Kansas (KU), the KU New Faculty General Research Fund, and the Center for Environmentally Beneficial Catalysis for generous support. The authors thank the National Science Foundation (Grant CHE-0079282) and the University of Kansas for funds to purchase the X-ray instrument and computers.

Supporting Information Available: Specific details of XRD data collection and analysis for **1-R** complexes (Tables S1−S5), CIF files for these complexes, molecular structures of isomers of **2-H** (Figure S1), space-filling models of **1-R** complexes based on XRD coordinates (Figure S2), Cartesian coordinates for all DFT energy-minimized models of **2-H** and **2-Me** (Tables S6−S8), room-temperature magnetic susceptibilities for **1-R** complexes (Table S9), ESI-MS data collected for **2-H** (Figure S3), experimental parameters obtained from a Gaussian deconvolution of electronic absorption and MCD data collected for **2-H** and **2-Me** (Tables S10 and S11), VTVH MCD simulations for **2-H** (Figure S4), details of DFT and TD-DFT computations for **2-H** and **2-Me** (Tables S12−S14), and plots of $d-d$ and CT transition energies as a function of $Mn-O_{peroxo}$ and O−O bond lengths, respectively (Figures S5 and S6). This material is available free of charge via the Internet at http://pubs.acs.org.

JA910235G